doi.org/10.36721/PJPS/2026.40.15558.1

Silica nanoparticle-delivered astragaloside IV promotes oxidative stress and apoptosis in prostate cancer cells via the miR-125-5p/STIR4 axis

Chungping Yang*, Peihsin Shie and Zhenye Xu
College of Tea and Food Science, WUYI University, Nanping, Fujian, 354300, China

Abstract: **Background**: Prostate cancer (PCa) treatment is limited by drug resistance and toxicity. Astragaloside IV (AIV) has anti-tumor activity but poor bioavailability. **Objectives**: To prepare silica nanoparticle-loaded astragaloside IV (SN-AIV) and to investigate whether it induces oxidative stress and apoptosis in PC-3 cells via the miR-125-5p/STIR4 axis. **Methods**: SN-AIV was prepared and characterized. PC-3 cells were treated with SN-AIV, free AIV, or controls. Cell viability, apoptosis, mitochondrial function and oxidative stress markers were assessed. qRT-PCR and Western blot detected miR-125-5p and STIR4 expression. A dual-luciferase reporter assay confirmed target binding. Functional rescue experiments were performed. **Results**: SN-AIV exhibited uniform size (98.4 ± 6.2 nm) and sustained release. Compared with controls, SN-AIV significantly reduced cell viability, induced apoptosis, decreased mitochondrial membrane potential, increased MDA and decreased SOD and GSH levels. SN-AIV up-regulated miR-125-5p and down-regulated STIR4. STIR4 was confirmed as a direct target of miR-125-5p. miR-125-5p overexpression or STIR4 knockdown mimicked SN-AIV effects, while miR-125-5p inhibition reversed them. **Conclusion**: SN-AIV induces oxidative stress and apoptosis in PC-3 cells by up-regulating miR-125-5p and down-regulating STIR4, providing an experimental basis for nanoparticle-delivered AIV in PCa treatment.

Keywords: Astragaloside IV; miR-125-5P; Prostate cancer; Silica nanoparticles; STIR4

Submitted on 10-11-2025 – Revised on 07-04-2026 – Accepted on 20-08-2026

Article in Press

INTRODUCTION

Prostate cancer (PCa) is one of the most common malignancies in men, with both its incidence and mortality rates rising globally (Van Blarigan *et al*., 2025). Current treatment strategies for locally advanced or metastatic PCa include chemical castration or surgical castration combined with anti-androgen drugs or paclitaxel-based chemotherapy. However, radical surgery or external radiotherapy has a high failure rate in high-risk patients and conventional chemotherapeutic agents suffer from short circulation time *in-vivo*, low bioavailability and poor targeting, severely affecting patients' quality of life. Therefore, the development of novel, efficient and low-toxicity therapeutic strategies has become an important direction in PCa research.

In recent years, nanodrug delivery systems have shown significant application prospects in the diagnosis and treatment of urological tumors (Xiao *et al*., 2024). Compared with traditional therapeutic strategies, nanoparticles can achieve precise drug accumulation at tumor sites through enhanced permeability and retention (EPR) effects, surface ligand modification, and controlled release, thereby improving efficacy and reducing systemic toxicity (Tian *et al*., 2022). Among these, mesoporous silica nanoparticles, owing to their good biocompatibility, tunable physicochemical properties and high drug-loading as drug delivery carriers and hold significant potential in the treatment of solid tumors such as prostate cancer (Djayanti *et al*., 2023; Tavakoli *et al*., 2026).

Astragaloside IV, one of the main active components of the traditional Chinese medicine *Astragalus membranaceus*, exhibits various pharmacological activities including antioxidant, anti-inflammatory, anti-fibrotic and anti-tumor effects (Zhu *et al*., 2025). In recent years, the role of Astragaloside IV in prostate cancer therapy has garnered increasing attention. Studies have found that Astragaloside IV enhances the sensitivity of prostate cancer cells to carboplatin by inhibiting the AKT/NF-κB signaling pathway (You *et al*., 2022) and suppresses proliferation and induces apoptosis in prostate cancer cells by downregulating KPNB1 expression (Ma *et al*., 2024). Furthermore, Astragaloside IV promotes pyroptosis in prostate cancer cells by reducing RAGE mRNA levels and decreasing the expression of NF-κB, TNF-α and IL-6 (You *et al*., 2024). These studies indicate that Astragaloside IV possesses multi-target, multi-pathway anti-prostate cancer activity, although its specific molecular mechanisms remain to be further elucidated.

MicroRNAs (miRNAs) are a class of non-coding small RNAs of 18–25 nucleotides in length that regulate various biological processes, including cell proliferation, apoptosis and migration, by modulating target gene expression at the post-transcriptional level. miR-125-5p is

**Corresponding author:* e-mail: cpyang@wuyiu.edu.cn

an important member of the miR-125 family and is aberrantly expressed in various tumors, where it plays critical regulatory roles. In prostate cancer, miR-125a-5p is upregulated in prostate cancer cell lines and clinical tissues; knockdown of miR-125a-5p inhibits prostate cancer cell proliferation and migration by targeting NAIF1 and caspase-3, suggesting that miR-125-5p may act as an oncogene in prostate cancer (Cong *et al*., 2025). STIR4 (SIP-CARF-containing TIR domain-containing protein 4) is a member of the TIR domain-containing protein family, which plays important roles in regulating apoptosis and inflammatory responses (Leibler *et al*., 2025). Currently, the expression pattern and function of STIR4 in prostate cancer have not been reported. Bioinformatics predictions have revealed that the seed sequence of miR-125-5p has conserved complementary binding sites within the 3'UTR region of the STIR4 gene (Huang *et al*., 2023), suggesting that STIR4 is a potential downstream target gene of miR-125-5p. Given the known functions of TIR family proteins in regulating apoptosis, STIR4 may be involved in oxidative stress and apoptosis in prostate cancer cells.

Although these clues suggest that miR-125-5p and STIR4 may be involved in the development and progression of prostate cancer, whether silica nanoparticles loaded with Astragaloside IV induce oxidative stress and apoptosis in prostate cancer cells by regulating the miR-125-5p/STIR4 axis remains unclear. Based on this, the following hypothesis was proposed in the present study: Silica nanoparticle-loaded Astragaloside IV (SN-AIV) can induce oxidative stress and apoptosis in prostate cancer PC-3 cells by upregulating miR-125-5p expression and inhibiting its downstream target gene STIR4. By preparing and characterizing Astragaloside IV-loaded silica nanoparticles (SN-AIV), the effects of SN-AIV were intended to be observed on oxidative stress and apoptosis in PC-3 cells and to validate the role of the miR-125-5p/STIR4 axis in the cellular effects induced by SN-AIV. A new theoretical basis will be provided by this study and an experimental foundation for nanomaterial-based targeted therapy of prostate cancer using active ingredients from traditional Chinese medicine. The research approach is illustrated in figure 1.

MATERIALS AND METHODS

Research materials

The human prostate cancer cell line PC-3 was purchased from the Laboratory Animal Center of WUYI University (Nanping, China). The DU145 cell line and the normal human prostate epithelial cell line RWPE-1 were obtained from the Cell Bank of the Typical Culture Collection Committee of the Chinese Academy of Sciences (Shanghai, China). The catalog numbers for PC-3, DU145, and RWPE-1 were CL-0158, CL-0099, and CL-0225, respectively (Procell Life Science & Technology Co., Ltd., Wuhan, China). All cell lines were authenticated by STR profiling, tested negative for mycoplasma, and used within passages 5–10.

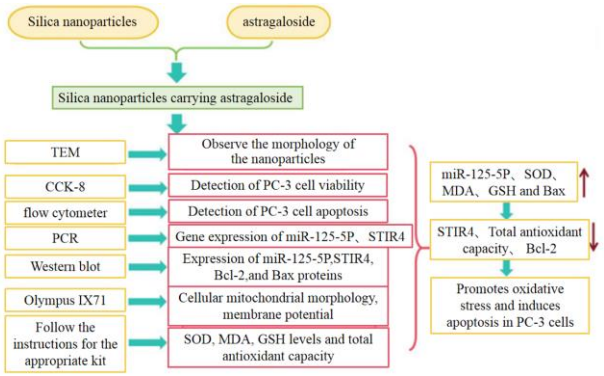


Fig. 1: SN-AIV promotes oxidative stress and apoptosis in PC-3 cells by up-regulating the expression of miR-125-5p and down-regulating the activity of the STIR4 pathway.

Astragaloside IV (purity ≥98%, batch No. B20564-20mg) was purchased from Shanghai Yuanye Biotechnology Co., Ltd. (Shanghai, China); its chemical structure is shown in fig. 2. The raw materials for preparing silica nanoparticles, including tetraethyl orthosilicate (TEOS), ammonia solution, ethanol, etc., were of analytical grade and purchased from Sinopharm Chemical Reagent Co., Ltd. (Shanghai, China).

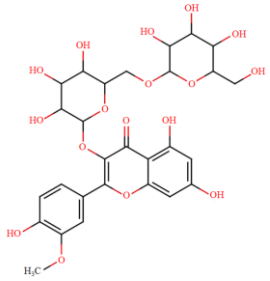


Fig. 2: Structural formula of astragaloside IV.

Main reagents and their sources: CCK-8 cell viability assay kit (Wuhan GeneCreate Biological Engineering Co., Ltd., Wuhan, China); Annexin V-FITC/PI apoptosis detection kit (Wuhan Pricella Biotechnology Co., Ltd., Wuhan, China); JC-1 mitochondrial membrane potential assay kit, total superoxide dismutase (T-SOD) assay kit (WST-8 method), malondialdehyde (MDA) assay kit (TBA method), reduced glutathione (GSH) assay kit (DTNB method), total antioxidant capacity (T-AOC) assay kit (FRAP method), RIPA lysis buffer and BCA protein assay kit (Beyotime Institute of Biotechnology, Shanghai, China). STIR4 antibody (ab235678, 1:1000), Bcl-2 antibody (ab32124, 1:1000), Bax antibody

Article in Press

(ab32503, 1:1000) and β-actin antibody (ab8226, 1:3000) were purchased from Abcam (USA). HRP-conjugated goat anti-rabbit secondary antibody (1:5000) was purchased from Cell Signaling Technology (USA).

Lipofectamine 3000 transfection reagent, TRIzol reagent and SYBR Green Master Mix were purchased from Invitrogen (USA). miR-125-5p mimic, anti-miR-125-5p, si-STIR4 and corresponding negative controls were synthesized by Guangzhou RiboBio Co., Ltd. (Guangzhou, China). All primers were synthesized by Sangon Biotech (Shanghai) Co., Ltd. (Shanghai, China).

Preparation and characterization of nanoparticles

Preparation of SN-AIV

Silica nanoparticles loaded with Astragaloside IV were prepared using the sol-gel method. An appropriate amount of Astragaloside IV was dissolved in distilled water to prepare a 20 mg/mL Astragaloside IV solution. 2.5 mL of tetraethyl orthosilicate (TEOS) was added to 30 mL of anhydrous ethanol and the mixture was stirred until dissolved. Then, an appropriate amount of ammonia solution was added to adjust the pH to 10.0 and magnetic stirring (Model MS-H-S, DLAB Scientific Co., Ltd., Beijing, China) was continued for 30 min to form a uniform silica precursor solution. Under magnetic stirring, Astragaloside IV solution was slowly added dropwise to the silica precursor solution at 0.5 mL/min, and the reaction was allowed to proceed at room temperature under continuous stirring for 24 h. After the reaction, the nanoparticles were collected by centrifugation (Model 5804 R, Eppendorf AG, Hamburg, Germany) at 12,000 × g for 30 min, washed three times each with anhydrous ethanol and distilled water and then freeze-dried (Model Alpha 1-2 LDplus, Martin Christ Gefriertrocknungsanlagen GmbH, Osterode am Harz, Germany)to obtain SN-AIV powder (Chien *et al*., 2022). Empty silica nanoparticles (SN) were prepared using the same method without the addition of Astragaloside IV.

Characterization of SN-AIV

Particle size and zeta potential: An appropriate amount of SN-AIV was dispersed in ultrapure water and the hydrodynamic particle size, polydispersity index (PDI) and zeta potential were measured using a Zetasizer Nano ZS90 laser particle size analyzer (Model ZEN3690, Malvern Panalytical Ltd., Malvern, UK).

Morphological observation: A small amount of SN-AIV dispersion was dropped onto a copper grid-supported film, naturally dried and then observed using a transmission electron microscope (TEM, Model JEM-1400Flash, JEOL Ltd., Tokyo, Japan) at an accelerating voltage of 80 kV.

Encapsulation efficiency and drug loading capacity: Astragaloside IV content was determined by high-performance liquid chromatography (HPLC, Model 1260 Infinity II, Agilent Technologies, Santa Clara, CA, USA) equipped with a diode array detector (DAD) (Chien *et al*., 2022). The chromatographic conditions were as follows: C18 column (4.6 mm × 250 mm, 5 μm, Model ZORBAX Eclipse XDB-C18, Agilent Technologies, Santa Clara, CA, USA), mobile phase of acetonitrile-water (35:65), flow rate of 1.0 mL/min and detection wavelength (λmax) of 203 nm. After centrifugation of SN-AIV, the supernatant was collected to determine the amount of unencapsulated drug. Encapsulation efficiency (%) = (Total drug amount – Drug amount in supernatant) / Total drug amount × 100%. Drug loading capacity (%) = (Drug amount in SN-AIV / Total mass of SN-AIV) × 100%.

In vitro release behavior: SN-AIV was dispersed in PBS buffer (pH 7.4 and 5.5) containing 10% fetal bovine serum and incubated in a constant-temperature shaker (Model MaxQ 6000, Thermo Fisher Scientific, Waltham, MA, USA) at 100 r/min and 37°C. At preset time points (0, 1, 2, 4, 6, 8, 12, 24, 48 h), the samples were centrifuged, the supernatant was collected and HPLC (Model 1260 Infinity II, Agilent Technologies, Santa Clara, CA, USA) was used to determine the amount of released drug at a detection wavelength (λmax) of 203 nm to calculate the cumulative release rate

Colloidal stability: SN-AIV was dispersed in RPMI 1640 medium containing 10% fetal bovine serum and incubated at 37°C. At 0, 6, 12, 24, and 48 h, particle size was measured using the Zetasizer Nano ZS90 (Model ZEN3690, Malvern Panalytical Ltd., Malvern, UK) to evaluate colloidal stability.

Determination of astragaloside IV working concentration

The appropriate working concentration of Astragaloside IV for subsequent experiments was determined using the CCK-8 assay. PC-3 cells were seeded into 96-well plates at 5×10^3 cells/well. After 24 h of culture, free Astragaloside IV at final concentrations of 0, 30, 60, 90, 120, 150 and 180 μmol/L was added. After 24 h of treatment, CCK-8 reagent was added, and the plates were incubated for an additional 1 h. Absorbance was measured at 450 nm using a microplate reader (Model Epoch 2, BioTek Instruments, Inc., Winooski, VT, USA) to calculate cell viability. Based on preliminary experimental results, the concentration that achieved an inhibition rate of approximately 20%–30% (i.e., cell viability reduced to 70%–80% of the control group) was selected as the working concentration. The results showed that 120 μmol/L Astragaloside IV inhibited by 24.6%, within the target range. Therefore, 120 μmol/L was determined as the working concentration for free Astragaloside IV in subsequent experiments. The concentration of SN-AIV was normalized based on the Astragaloside IV content.

Article in Press

Cell culture and experimental grouping

Cell culture and transfection

PC-3 cells, DU145 cells and RWPE-1 cells were cultured in RPMI 1640 medium supplemented with 10% fetal bovine serum, 100 U/mL penicillin and 100 μg/mL streptomycin, in a constant temperature incubator (Model HERAcell 150i, Thermo Fisher Scientific, Waltham, MA, USA) at 37°C with 5% CO□. The medium was changed every 2–3 days and cells were passaged when they reached 80%–90% confluence. All experiments were performed with cells in the logarithmic growth phase, and cell confluence was maintained at 60%–70% before experimentation. Cell transfection was performed using Lipofectamine 3000 transfection reagent. Cells were seeded into 6-well plates 24 h before transfection to achieve 50%–60% confluence at the time of transfection. The transfection system was prepared according to the manufacturer's instructions. The final concentrations of the transfection reagents were: 50 nmol/L for miR-125-5p mimic and anti-miR-125-5p and 100 nmol/L for si-STIR4. Cells were harvested 48 h after transfection for subsequent experiments. Transfection efficiency was verified by qRT-PCR.

Experimental grouping

Effects of SN-AIV on PC-3 cells: Control group: PC-3 cells cultured routinely without any treatment. Empty vector control group (SN): PC-3 cells treated with an equal amount of unloaded blank silica nanoparticles. Positive control group (H_2O_2): PC-3 cells treated with 200 μmol/L H_2O_2 for 24 h as a positive control for oxidative stress and apoptosis. Free drug group (AIV): PC-3 cells treated with 120 μmol/L free Astragaloside IV for 24 h. Nanodrug group (SN-AIV): PC-3 cells treated with SN-AIV for 24 h (120 μmol/L based on Astragaloside IV content).

Effects of miR-125-5p and STIR4 on PC-3 cells: miR-NC group: Transfected with miR-125-5p mimic negative control. miR-125-5p mimic group: Transfected with miR-125-5p mimic. si-NC group: Transfected with STIR4 small interfering RNA negative control. si-STIR4 group: Transfected with small interfering RNA targeting STIR4.

Functional validation of miR-125-5p in the effect of SN-AIV: SN-AIV + anti-miR-NC group: PC-3 cells were transfected with anti-miR-NC for 48 h, then treated with SN-AIV for 24 h. SN-AIV + anti-miR-125-5p group: PC-3 cells were transfected with anti-miR-125-5p for 48 h, then treated with SN-AIV for 24 h. Three replicate wells were set up for each group and all experiments were independently repeated three times.

Cell viability detection

Cell viability was detected using the CCK-8 assay. After treatment of each group, 10 μL of CCK-8 reagent was added to each well and incubated at 37°C in the dark for 1 h. The absorbance was measured at 450 nm using a microplate reader (Model Epoch 2, BioTek Instruments, Inc., Winooski, VT, USA). Cell viability (%) = (Absorbance of experimental group – Absorbance of blank group) / (Absorbance of control group – Absorbance of blank group) × 100%. Three replicate wells were set up for each group and the experiment was independently repeated three times.

Apoptosis detection

Apoptosis was detected using the Annexin V-FITC/PI double staining method. After treatment for each group, cells were collected by trypsinization (0.25% trypsin), washed twice with PBS, and resuspended in 500 μL of Binding Buffer at a density of 1×10^6 cells/mL. Then, 5 μL of Annexin V-FITC was added and the cells were incubated at room temperature in the dark for 10 min, Flow cytometry (Model FACSCalibur, BD Biosciences, San Jose, CA, USA) was performed, collecting 10,000 events per sample. The proportions of early- and late-apoptotic cells were analyzed using FlowJo software (Version 10.8, BD Biosciences, San Jose, CA, USA). The H_2O_2 (200 μmol/L, 24 h) treatment group served as a positive control for apoptosis and untreated cells served as a negative control to ensure the reliability of the detection system.

PCR detection

Total RNA was extracted from PC-3 cells in each group using TRIzol. The A260/A280 ratio was between 1.8 and 2.0 as measured by UV spectrophotometry (Model NanoDrop 2000, Thermo Fisher Scientific, Waltham, MA, USA) , and 1.5% agarose gel electrophoresis showed clear, intact 28S and 18S bands, confirming that the RNA quality met the requirements. cDNA was synthesized by reverse transcription using PrimeScript RT Master Mix. qRT-PCR was performed using SYBR Green Master Mix on an ABI 7500 Real-Time PCR system (Model 7500, Applied Biosystems, Foster City, CA, USA). The reaction conditions were: 95°C for 3 min for initial denaturation; 40 cycles of 95°C for 10 s (denaturation) and 60°C for 30 s (annealing/extension). A melting curve analysis was performed after the reaction and each gene showed a single sharp peak, confirming good primer specificity. U6 was used as the internal reference gene for miR-125-5p and β-actin was used as the internal reference gene for STIR4. Preliminary experiments confirmed stable expression of both in all treatment groups (Ct value standard deviation < 0.5). The relative gene expression was calculated using the $2^{-\Delta\Delta Ct}$ method. All primers were validated by conventional PCR and the amplification products showed a single band of the expected size on 2% agarose gel electrophoresis. Melting curve analysis after qRT-PCR showed a single sharp peak for each gene. The primer sequences were as follows: miR-125-5p: Forward 5′-TCCCTGAGACCCTAACTTGTG-3′, Reverse 5′-AGTCTCAGGGTCCGAGGTATTC-3′. U6: Forward 5′-

Article in Press

CTCGCTTCGGCAGCACA-3′, Reverse 5′-AACGCTTCACGAATTTGCGT-3′. STIR4: Forward 5′-CGCTTATTGAAGCCAGCACT-3′, Reverse 5′-TTATCCAGGCAAACCATGTG-3′. β-actin: Forward 5′-CAGGTGTGGACGGGG-3′, Reverse 5′-GGGAGGCAG-3′.

Western blot

PC-3 cells were lysed on ice for 30 min using RIPA lysis buffer containing protease and phosphatase inhibitors, then centrifuged (Model 5804 R, Eppendorf AG, Hamburg, Germany) at 12,000 × g for 15 min at 4°C and the supernatant was collected. Protein concentration was determined using the BCA method. Equal amounts of protein (30 μg/lane) were mixed with 5× SDS loading buffer and denatured at 100°C for 10 min. After separation by 10% SDS-PAGE using a gel electrophoresis system (Model Mini-PROTEAN Tetra, Bio-Rad Laboratories, Inc., Hercules, CA, USA) , the proteins were transferred to PVDF membranes using a wet transfer system (Model Trans-Blot Turbo, Bio-Rad Laboratories, Inc., Hercules, CA, USA) at 250 mA for 90 min. . After transfer, Ponceau S staining was used to assess transfer efficiency and confirm consistent loading across lanes. The membranes were blocked with 5% non-fat milk at room temperature for 1 h, then incubated with primary antibodies (STIR4, 1:1000; Bcl-2, 1:1000; Bax, 1:1000; β-actin, 1:3000) overnight at 4°C. After washing three times with TBST, the membranes were incubated with HRP-conjugated secondary antibody (1:5000) at room temperature for 1 h. The signals were visualized using an enhanced chemiluminescence (ECL) method with a chemiluminescence imaging system (Model ChemiDoc MP, Bio-Rad Laboratories, Inc., Hercules, CA, USA) . ImageJ software (Version 1.53, National Institutes of Health, Bethesda, MD, USA) was used to analyze the grayscale values of the protein bands, with β-actin as the internal control for quantification. The relative expression level of the target protein = grayscale value of target protein / grayscale value of β-actin. The H_2O_2 (200 μmol/L, 24 h) treatment group served as a positive control for the detection of apoptosis-related proteins. Three replicate wells were set up for each group and the experiment was independently repeated three times.

Mitochondrial membrane potential detection

Mitochondrial membrane potential was detected using the JC-1 fluorescent probe. After treatment for each group, the medium was discarded, and the cells were washed once with PBS. A JC-1 working solution was added, and the cells were incubated at 37°C in the dark for 20 min. After incubation, cells were washed twice with JC-1 staining buffer. Images were observed and captured using a confocal laser scanning microscope (Model TCS SP8, Leica Microsystems GmbH, Wetzlar, Germany). JC-1 aggregates (red fluorescence, excitation 585 nm, emission 590 nm) and JC-1 monomers (green fluorescence, excitation 514 nm, emission 529 nm) were visualized and the ratio of red to green fluorescence intensity reflected the level of mitochondrial membrane potential. Cells treated with 10 μmol/L CCCP for 30 min served as a positive control for complete depolarization of the mitochondrial membrane potential. Five random fields of view were selected for analysis per group.

Detection of oxidative stress markers

After treatment of PC-3 cells in the above groups, the following indicators were detected according to the instructions of the corresponding kits (Beyotime, China): (1) Total superoxide dismutase (T-SOD) activity using the WST-8 method (detection wavelength 450 nm); (2) Malondialdehyde (MDA) content using the thiobarbituric acid (TBA) method (detection wavelength 532 nm); (3) Reduced glutathione (GSH) content using the DTNB method (detection wavelength 412 nm); (4) Total antioxidant capacity (T-AOC) using the FRAP (ferric reducing ability of plasma) method (detection wavelength 593 nm), calculated using an $FeSO_4$ standard curve. All absorbance measurements were performed using a microplate reader (Model Epoch 2, BioTek Instruments, Inc., Winooski, VT, USA). Three replicate wells were set up for each group and all experiments were independently repeated three times.

Dual-luciferase reporter gene assay

To verify the direct targeting regulation of STIR4 by miR-125-5p, dual-luciferase reporter plasmids containing the wild-type (WT) and mutant (MUT) sequences of the STIR4 3'UTR were constructed. PC-3 cells were seeded into 24-well plates (5×10^4 cells/well). The reporter plasmid (100 ng/well) and miR-125-5p mimic or miR-NC (50 nmol/L) were co-transfected using Lipofectamine 3000. After 48 h of transfection, firefly luciferase and Renilla luciferase activities were measured using a dual-luciferase reporter assay kit (Model E1910, Promega Corporation, Madison, WI, USA) and a luminometer (Model GloMax 20/20, Promega Corporation, Madison, WI, USA). The ratio of firefly to Renilla luciferase activity was calculated as the relative luciferase activity.

Statistical analysis

Statistical analysis was performed using SPSS 26.0 and GraphPad Prism 9.0 software. All data are presented as mean ± standard deviation (SD). The data followed a normal distribution and had homogeneity of variance. Comparisons among multiple groups were performed using one-way analysis of variance (ANOVA), followed by Tukey's HSD test for multiple comparison correction. Comparisons between two groups were performed using an independent samples t-test. A P-value < 0.05 was considered statistically significant. The sample size (n=6) was calculated based on the effect size from preliminary experiments (Cohen's $d = 1.2$) with $\alpha = 0.05$ and $\beta = 0.2$. All experiments were independently repeated three times.

Article in Press

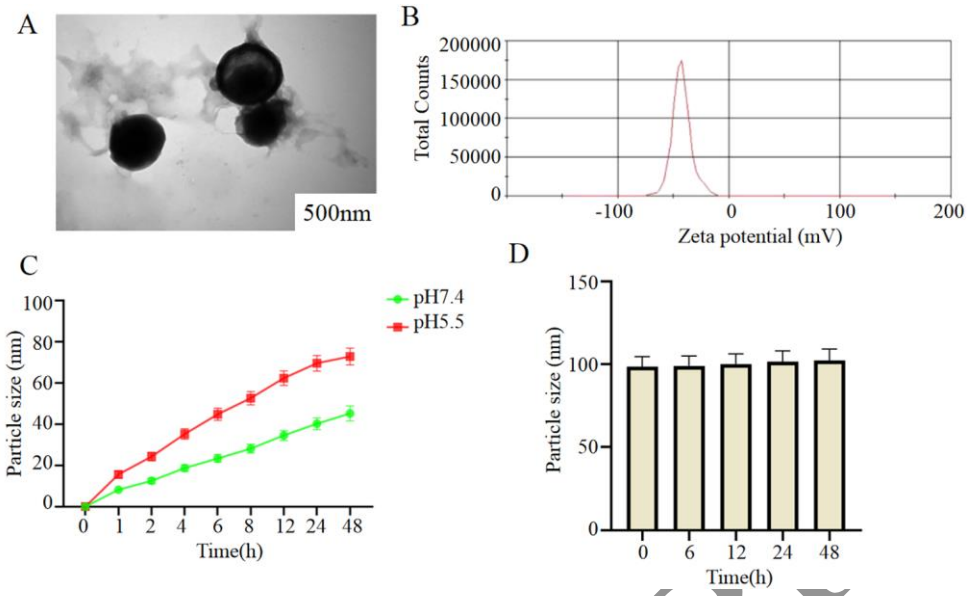


Fig. 3: Characterization of SN-AIV. (A) TEM image of SN-AIV(scale bar = 500 nm); (B) Zeta potential distribution of SN-AIV; (C) Cumulative release profiles of SN-AIV at pH 7.4 and pH 5.5. Data are presented as mean ± SD (n = 3); (D) Colloidal stability of SN-AIV in culture medium containing 10% fetal bovine serum, showing no significant change in particle size within 48 h (n = 3).

The data in the figures are presented as mean ± SD, with individual data points indicated to reflect the data distribution.

RESULTS

Successful preparation of SN-AIV

Silica nanoparticles loaded with Astragaloside IV (SN-AIV) were successfully prepared. Transmission electron microscopy results showed that SN-AIV exhibited a uniform spherical shape with homogeneous particle size, good dispersibility and no obvious aggregation (Fig. 3A). Dynamic light scattering results showed that the average hydrodynamic particle size of SN-AIV was 98.4 ± 6.2 nm, the polydispersity index (PDI) was 0.12 ± 0.03 and the zeta potential was -42.3 ± 3.1 mV (Fig. 3B), indicating good colloidal stability of the nanoparticles. High-performance liquid chromatography results showed that the encapsulation efficiency of SN-AIV was 78.6 ± 4.2% and the drug loading capacity was 12.3 ± 1.1%. *In-vitro* release assay results (Fig. 3C) showed that the cumulative release rate of SN-AIV at pH 7.4 was 45.2 ± 3.6% over 48 h; at pH 5.5, the cumulative release rate was 72.8 ± 4.1%, exhibiting acidic environment-responsive release characteristics. Colloidal stability assay results (Fig. 3D) showed that after incubation of SN-AIV in culture medium containing 10% fetal bovine serum for 48 h, the particle size did not change significantly ($P > 0.05$), indicating good stability under physiological conditions.

SN-AIV inhibits PC-3 cell viability and induces apoptosis

CCK-8 results showed that, compared with the Control group, cell viability in the SN group did not differ significantly ($P > 0.05$), whereas cell viability in the H_2O_2 positive control group, AIV group, and SN-AIV group was significantly reduced ($P < 0.001$). Compared with the AIV group, cell viability in the SN-AIV group was further reduced ($P < 0.01$), indicating that SN-AIV more effectively inhibited PC-3 cell viability (Fig. 4A).

Flow cytometry results showed no significant difference in apoptosis rate between the Control and SN groups ($P > 0.05$). The apoptosis rates in the H□O□ group, AIV group and SN-AIV group were significantly higher than that in the Control group ($P < 0.001$), with the SN-AIV group showing the highest apoptosis rate, which was significantly higher than that of the AIV group ($P < 0.01$) (Fig. 4B).

SN-AIV induces mitochondrial dysfunction in PC-3 cells

JC-1 staining results showed no significant difference in mitochondrial membrane potential (red/green fluorescence ratio) between the Control group and the SN group ($P > 0.05$). The red/green fluorescence ratio in the CCCP positive control group was significantly reduced ($P < 0.001$). The red/green fluorescence ratios in both the AIV group and the SN-AIV group were significantly lower than those in the Control group ($P < 0.001$) and the ratio in the SN-AIV group was lower than that in the AIV group ($P < 0.01$), indicating that SN-AIV more significantly reduced mitochondrial membrane potential (Fig. 4C). Mitotracker staining results showed that in the Control group and SN group, mitochondria exhibited elongated filamentous structures forming a continuous mitochondrial network.

Article in Press

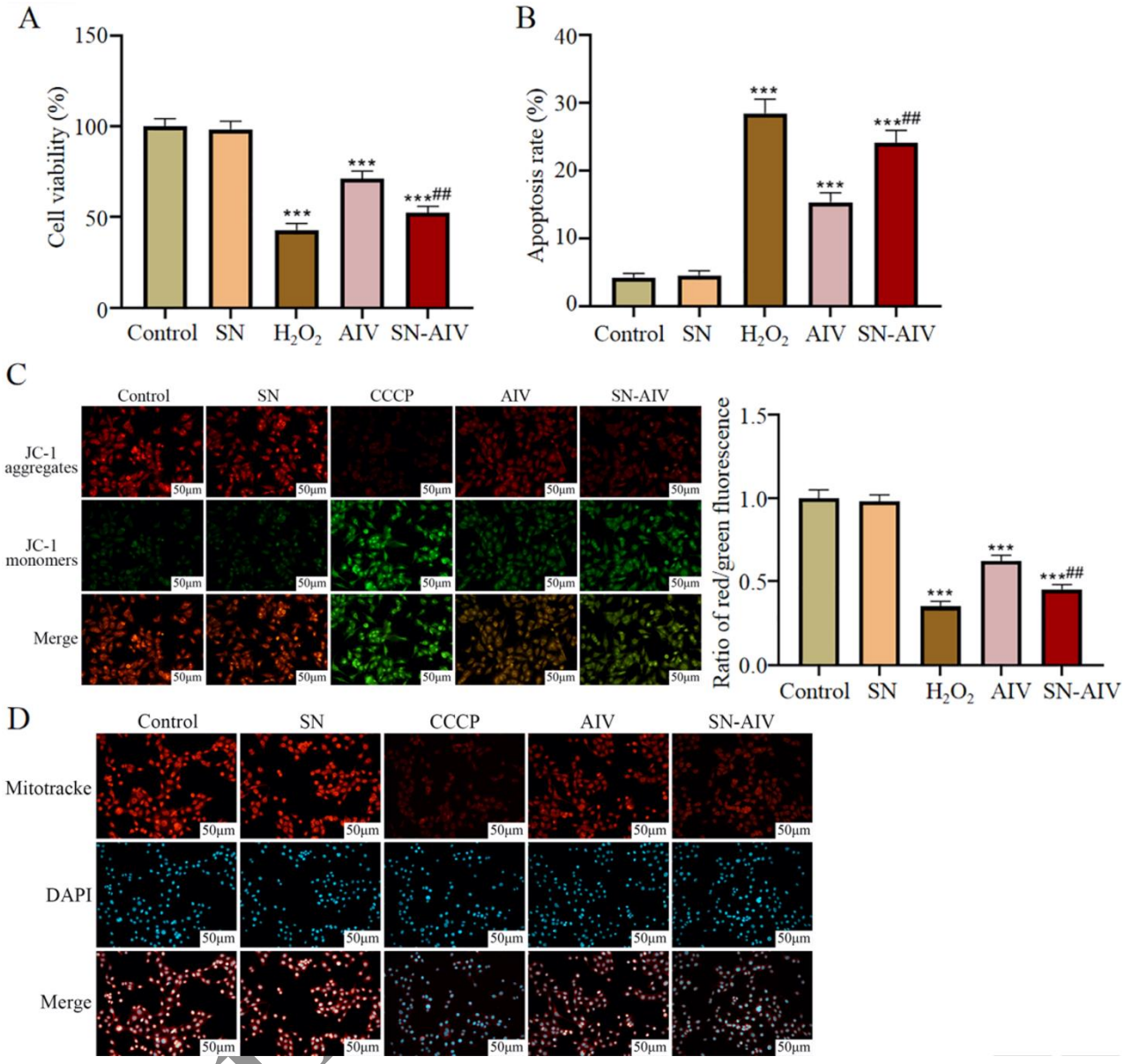


Fig. 4: Effects of SN-AIV on PC-3 cell viability, apoptosis and mitochondrial function. (A) CCK-8 assay was used to detect PC-3 cell viability in each group (n = 6), normalized to 100% of the Control group; (B) Flow cytometry was used to detect the apoptosis rate of PC-3 cells in each group (n = 6); (C) JC-1 staining was used to detect mitochondrial membrane potential (scale bar = 10 μm), expressed as the red/green fluorescence ratio (n = 6). CCCP (10 μmol/L, 30 min) served as a positive control; (D) Mitotracker staining was used to observe mitochondrial morphology (scale bar = 20 μm). Data are presented as mean ± SD.***P < 0.001 vs Control group; ##P < 0.01 vs AIV group.

In the AIV group, the mitochondrial network became shortened, appearing as dispersed, short, rod-like structures. In the SN-AIV group, mitochondrial fragmentation was more pronounced, appearing as punctate distributions, suggesting mitochondrial dynamics imbalance (Fig. 4D).

SN-AIV induces oxidative stress in PC-3 cells

Compared with the Control group, no significant changes in oxidative stress markers were observed in the SN group (P > 0.05). In the H_2O_2 positive control group, AIV group, and SN-AIV group, SOD activity, MDA content, and GSH levels were significantly increased, while total antioxidant capacity was significantly decreased (P < 0.001). Compared with the AIV group, the SN-AIV group showed a further exacerbation of oxidative stress (P < 0.01), indicating that SN-AIV induces greater oxidative stress in PC-3 cells (Fig. 5).

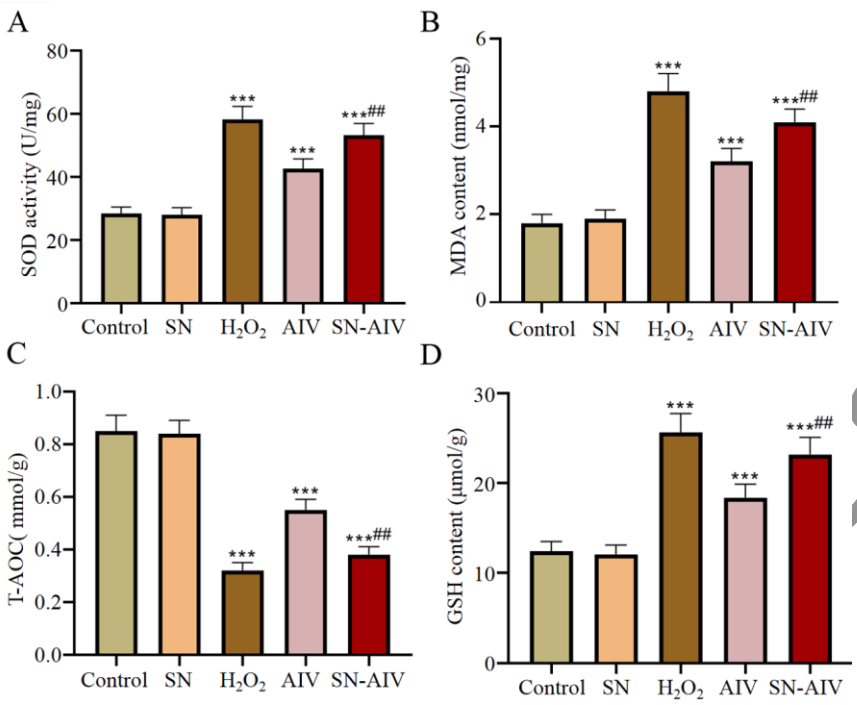


Fig. 5: Effects of SN-AIV on oxidative stress markers in PC-3 cells. (A) Total superoxide dismutase (SOD) activity; (B) Malondialdehyde (MDA) content; (C) Total antioxidant capacity (T-AOC); (D) Reduced glutathione (GSH) content. H□O□ (200 μmol/L, 24 h) served as a positive control. Data are presented as mean ± SD (n = 6). ***P < 0.001 vs Control group; ##P < 0.01 vs AIV group.

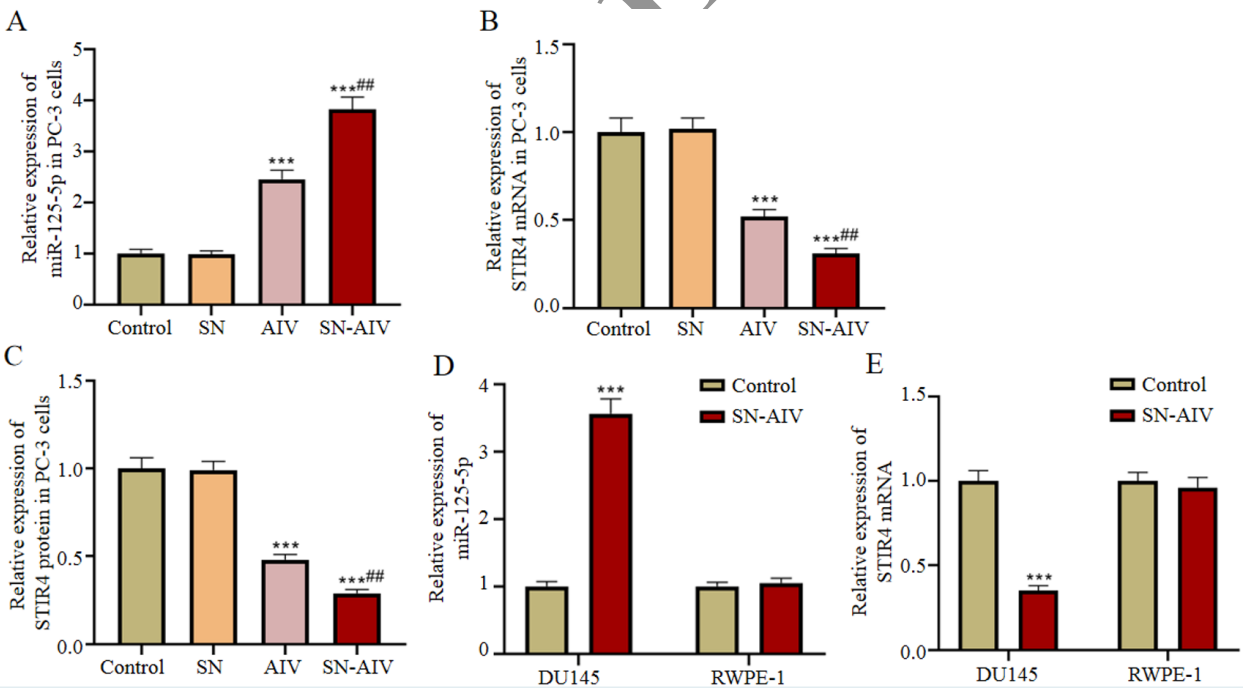


Fig. 6: Effects of SN-AIV on the miR-125-5p/STIR4 axis. (A) qRT-PCR was used to detect the expression level of miR-125-5p in PC-3 cells (n = 6); (B) qRT-PCR was used to detect the expression level of STIR4 mRNA in PC-3 cells (n = 6); (C) Western blot was used to detect the expression level of STIR4 protein in PC-3 cells (n = 3); (D) qRT-PCR was used to detect the expression level of miR-125-5p in DU145 and RWPE-1 cells (n = 6); (E) qRT-PCR was used to detect the expression level of STIR4 mRNA in DU145 and RWPE-1 cells (n = 6). Data are presented as mean ± SD. ***P < 0.001 vs Control group; ##P < 0.01 vs AIV group.

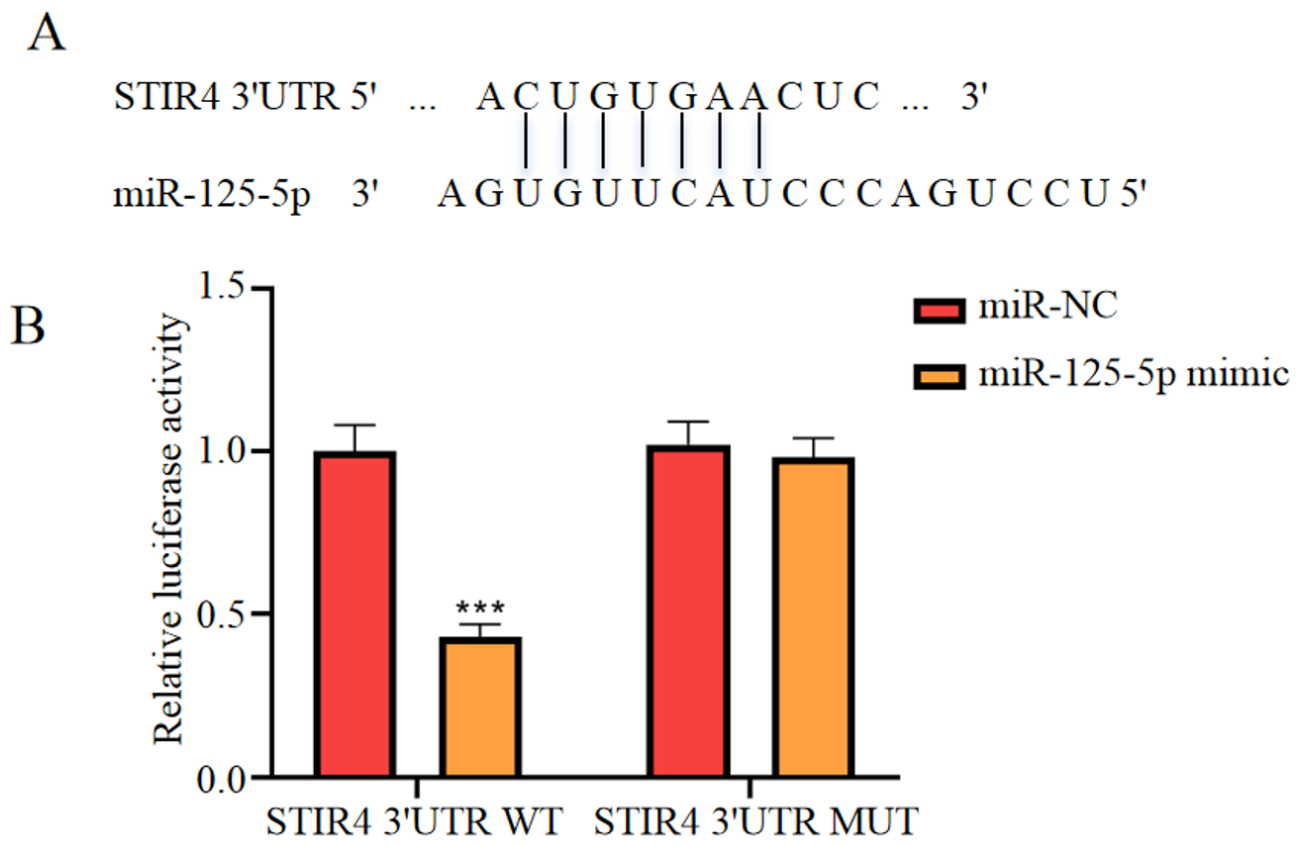


Fig. 7: miR-125-5p targets and regulates STIR4. (A) Schematic diagram showing the predicted binding sites between miR-125-5p and the STIR4 3′UTR; (B) Dual-luciferase reporter gene assay was used to detect the effect of miR-125-5p on the luciferase activity of STIR4 3′UTR wild-type (WT) and mutant (MUT) reporter plasmids (n = 6). Data are presented as mean ± SD. ***P < 0.001 vs miR-NC group.

SN-AIV upregulates miR-125-5p expression and downregulates STIR4 expression

qRT-PCR and Western blot results showed that compared with the Control group, no significant differences in miR-125-5p and STIR4 expression were observed in the SN group (P > 0.05). In the AIV group and SN-AIV group, miR-125-5p expression was significantly increased (P < 0.001), while STIR4 mRNA and protein expression were significantly decreased (P < 0.001). Compared with the AIV group, the SN-AIV group showed further increased miR-125-5p expression (P < 0.01) and further decreased STIR4 expression (P < 0.01) (Fig. 6). To further validate the generality of this regulatory relationship, verification was performed in DU145 prostate cancer cells and RWPE-1 normal prostate epithelial cells. The results showed that SN-AIV significantly upregulated miR-125-5p expression and downregulated STIR4 expression in DU145 cells (P < 0.001), but had no significant effect on their expression in RWPE-1 cells (P > 0.05) (Figs. 6D-E).

Validation of miR-125-5p targeting regulation of STIR4

Bioinformatics prediction showed that the seed sequence of miR-125-5p has conserved complementary binding sites with the 3′UTR region of the STIR4 gene (Fig. 7A). Dual-luciferase reporter gene assay results showed that after co-transfection of miR-125-5p mimic with STIR4 3′UTR wild-type reporter plasmid, luciferase activity was significantly reduced (P < 0.001); after transfection with the mutant reporter plasmid, luciferase activity showed no significant change (P > 0.05) (Fig. 7B), confirming that miR-125-5p directly targets and binds to the 3′UTR of STIR4.

miR-125-5p overexpression or STIR4 knockdown mimics the effects of SN-AIV

Effect of miR-125-5p overexpression

In PC-3 and DU145 cells, compared with the miR-NC group, the miR-125-5p mimic group showed significantly increased miR-125-5p expression (P < 0.001) and significantly decreased STIR4 expression (P < 0.001). After miR-125-5p overexpression, cell viability was significantly reduced (P < 0.001), apoptosis rate was significantly increased (P < 0.001), SOD, MDA and GSH levels were significantly increased and total antioxidant capacity was significantly decreased (P < 0.001), consistent with the effects observed in the SN-AIV treatment group (Fig. 8).

Article

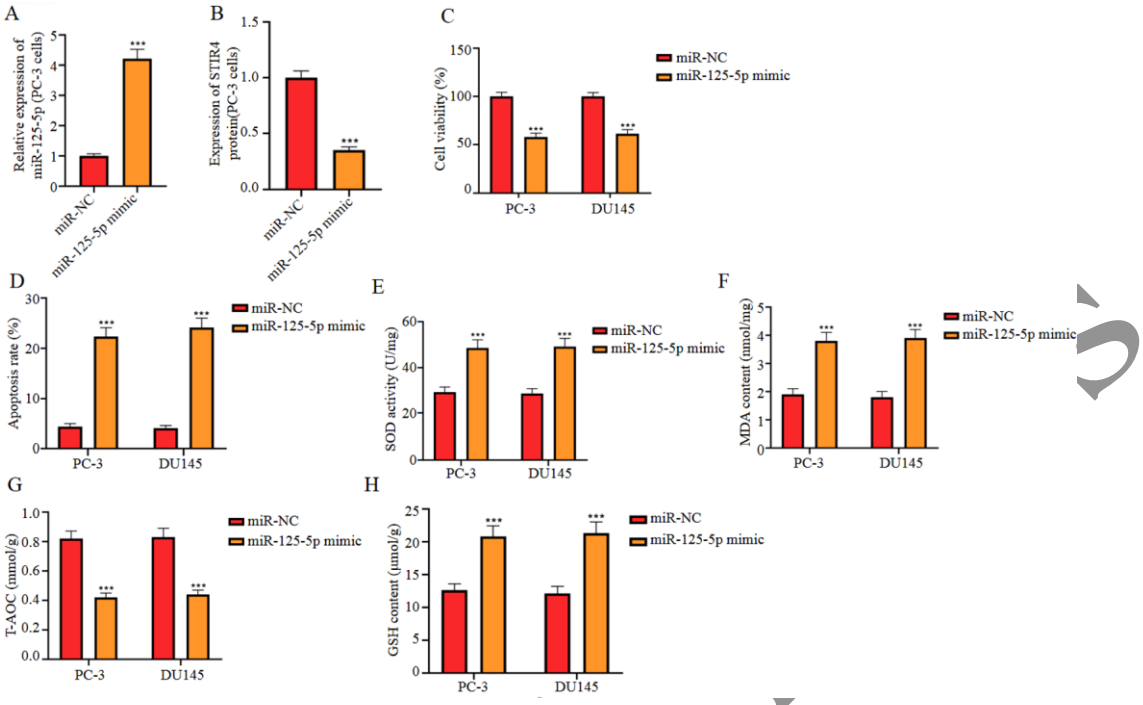


Fig. 8: Effects of miR-125-5p overexpression on PC-3 and DU145 cells. (A) miR-125-5p expression level; (B) STIR4 protein expression level; (C) Cell viability; (D) Apoptosis rate; (E) SOD activity; (F) MDA content; (G) Total antioxidant capacity; (H) GSH content. Data are presented as mean ± SD (n = 6). ***P < 0.001 vs miR-NC group.

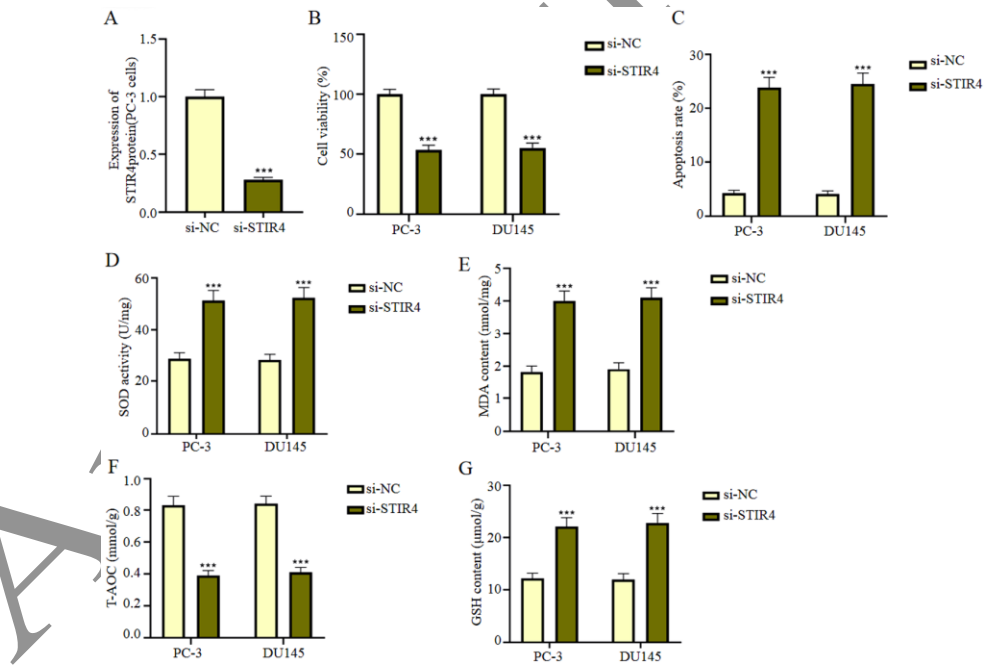


Fig. 9: Effects of STIR4 knockdown on PC-3 and DU145 cells. (A) STIR4 protein expression level; (B) Cell viability; (C) Apoptosis rate; (D) SOD activity; (E) MDA content; (F) Total antioxidant capacity; (G) GSH content. Data are presented as mean ± SD (n = 6). ***P < 0.001 vs si-NC group.

Effect of STIR4 knockdown

In PC-3 and DU145 cells, compared with the si-NC group, the si-STIR4 group showed significantly decreased STIR4 expression (P < 0.001). After STIR4 knockdown, cell viability was significantly reduced (P < 0.001), apoptosis rate was significantly increased (P < 0.001), SOD, MDA and GSH levels were significantly increased and total antioxidant capacity was significantly decreased (P < 0.001), consistent with the effects observed in the SN-AIV treatment group (Fig. 9).

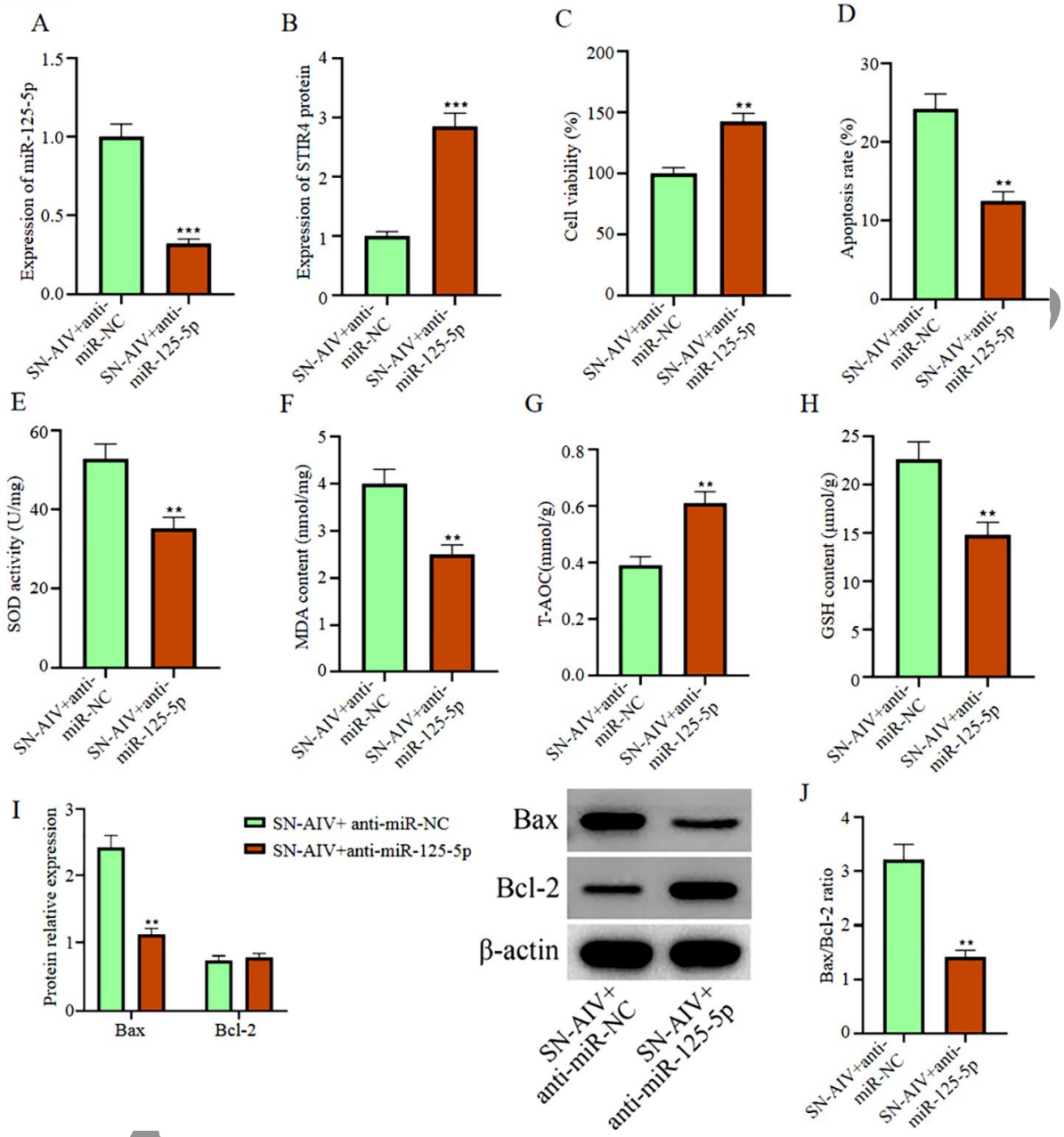


Fig. 10: Inhibition of miR-125-5p reverses the effects of SN-AIV. (A) miR-125-5p expression level; (B) STIR4 protein expression level; (C) Cell viability; (D) Apoptosis rate; (E) SOD activity; (F) MDA content; (G) Total antioxidant capacity; (H) GSH content; (I) Bax and Bcl-2 protein expression levels; (J) Bax/Bcl-2 ratio. Data are presented as mean ± SD (n = 6). **P < 0.01, ***P < 0.001 vs SN-AIV + anti-miR-NC group.

Effect on normal cells

In RWPE-1 normal prostate epithelial cells, miR-125-5p overexpression or STIR4 knockdown had no significant effect on cell viability, apoptosis, or oxidative stress markers ($P > 0.05$), suggesting that this regulatory axis is specific to prostate cancer cells.

Inhibition of miR-125-5p reverses the effects of SN-AIV

In PC-3 cells, the SN-AIV + anti-miR-NC group showed effects consistent with the SN-AIV alone treatment group. Compared with the SN-AIV + anti-miR-NC group, the SN-AIV + anti-miR-125-5p group showed significantly decreased miR-125-5p expression ($P < 0.001$), significantly increased STIR4 expression ($P < 0.001$), significantly increased cell viability ($P < 0.01$), significantly decreased apoptosis rate ($P < 0.01$), significantly decreased SOD, MDA and GSH levels, significantly increased total antioxidant capacity ($P < 0.01$) and a significantly decreased Bax/Bcl-2 ratio ($P < 0.01$), indicating that inhibition of miR-125-5p partially reverses the oxidative stress and apoptosis effects induced by SN-AIV (Fig. 10).

DISCUSSION

The pathogenesis of prostate cancer (PCa) is complex and existing treatment options for patients with advanced disease show limited efficacy and significant side effects, necessitating the development of novel therapeutic strategies. In recent years, the combination of nanodrug delivery systems and active ingredients from traditional Chinese medicine has shown promising prospects in cancer therapy (Fu *et al*., 2025). In this study, SN-AIV was successfully prepared and validated its ability to induce oxidative stress and apoptosis in PC-3 cells by regulating the miR-125-5p/STIR4 axis.

This study is the first to report that SN-AIV significantly upregulates miR-125-5p expression and downregulates the expression of its target gene STIR4, thereby inducing oxidative stress and apoptosis in PC-3 cells. Dual-luciferase reporter assays confirmed that STIR4 is a direct target of miR-125-5p. Further functional experiments showed that miR-125-5p overexpression or STIR4 knockdown mimicked the effects of SN-AIV, whereas miR-125-5p inhibition partially reversed these effects. These results indicate that the miR-125-5p/STIR4 axis plays a key regulatory role in the cellular effects induced by SN-AIV.

Current research on STIR4 has primarily focused on immune evasion (Vallejo-Schmidt et al., 2024; Klontz et al., 2023), and its function in tumors has not yet been reported. This study is the first to reveal that STIR4 is highly expressed in prostate cancer cells and participates in regulating cellular oxidative stress and apoptosis, expanding the research boundaries of the TIR domain-containing protein family in tumor biology. Meanwhile, the role of miR-125-5p in prostate cancer remains controversial. Some studies have reported that miR-125a-5p is upregulated in prostate cancer and promotes tumor progression (Sheng *et al*., 2022), whereas this study found that its induction by SN-AIV exerts anti-cancer effects. This discrepancy may arise from differences in cell types, regulatory networks, and intervention methods, suggesting that miR-125-5p may exhibit functional diversity across contexts.

Compared with free Astragaloside IV, SN-AIV exhibited stronger effects in inhibiting proliferation, inducing apoptosis and disrupting mitochondrial function at the same drug concentration. This enhanced effect may be attributed to the improved cellular uptake efficiency, the acidic microenvironment-responsive release, and the prolonged intracellular retention time conferred by its nanostructure (Zhu *et al*., 2025). The SN-AIV prepared in this study exhibited uniform particle size, good dispersibility, high colloidal stability and faster release behavior at pH 5.5, consistent with the characteristics of the tumor acidic microenvironment, reflecting the advantages of nanodelivery systems in improving drug efficacy.

Astragaloside IV has been used in the treatment of tumors such as breast cancer, lung cancer and gastric cancer, with mechanisms mostly involving antioxidant, anti-inflammatory and immunomodulatory effects (Zhu and Lu, 2024; Wu *et al*., 2024; Li *et al*., 2022). This study is the first to combine Astragaloside IV with silica nanoparticles for prostate cancer treatment, further expanding its application scope and providing a reference for the nanomodification of active ingredients from traditional Chinese medicine.

This study represents an initial cellular-level exploration and has the following limitations: First, all experiments were conducted in the prostate cancer PC-3 cell line. Although partial mechanisms were validated in DU145 cells, a systematic comparison across multiple cell lines and normal cells is lacking. Second, animal models have not been established to evaluate the *in-vivo* anti-tumor efficacy, biodistribution and safety of SN-AIV. Third, the downstream signaling pathways of STIR4 have not been thoroughly investigated and the specific mechanisms by which STIR4 mediates oxidative stress and apoptosis remain to be elucidated.

Future studies should further establish prostate cancer xenograft models to evaluate the in *vivo* efficacy and safety of SN-AIV. Combined with transcriptomics, proteomics, and other approaches, the molecular network underlying STIR4 regulation of oxidative stress should be systematically dissected. In addition, exploring the synergistic effects of SN-AIV combined with existing chemotherapy or immunotherapy will provide a stronger basis for its clinical translation.

CONCLUSION

In summary, this study successfully prepared silica nanoparticles loaded with Astragaloside IV (SN-AIV) and, for the first time, revealed the molecular mechanism by which SN-AIV induces oxidative stress and apoptosis in prostate cancer PC-3 cells through upregulating miR-125-5p and inhibiting STIR4 expression. Although this study is only at the cellular level, it provides a new experimental basis and research approach for nanoparticle-based targeted therapy of prostate cancer using active ingredients from traditional Chinese medicine.

Acknowledgments
None.

Authors' contributions
Chungping Yang: Conceptualized the research, designed the experimental methodology, supervised the entire research project, curated the data and reviewed and

Article in Press

finalized the manuscript; Peihsin Shie and Zhenye Xu: Performed the majority of the experiments, model establishment, data collection, initial draft preparation and participated in manuscript writing. All authors have read and approved the final version of the manuscript for submission and publication.

Funding
This work was supported by the Fujian Provincial Education and Scientific Research Project for Young and Middle-aged Teachers, No. JAT251176.

Data availability statement
The datasets generated during and/or analysed during the current study are available from the corresponding author on reasonable request.

Ethical approval
This study was approved by the ethnic committee of WUYI University (approval number: No. YJ202511). All cell lines are from commercial sources and do not require additional ethical reviews, but have been approved by institutions.

Conflict of interest
The authors declare no conflict of interest.

REFERENCES

Cong Z, Qiu D and Hu H (2025). Mendelian randomization reveals causal circulatory microRNAs in prostate cancer pathogenesis and prognosis. *Medicine (Baltimore)*., **104**(31): e43613.

Chien MY, Yang CM and Chen CH (2022). Effects of physical properties and processing methods on astragaloside IV and flavonoids content in astragali radix. *Molecules*., **27**(2): 575.

Djayanti K, Maharjan P, Cho KH, Jeong S, Kim MS, Shin MC and Min KA (2023). Mesoporous silica nanoparticles as a potential nanoplatform: Therapeutic applications and considerations. *Int. J. Mol. Sci*., **24**(7): 6349.

Fu Z, Wang S, Zhou X, Ouyang L, Chen Z and Deng G (2025). Harnessing the power of traditional Chinese medicine in cancer treatment: The role of nanocarriers. *Int J Nanomed*., **20**: 3147–3174.

Huang J, Wu X, Zhang Q, Yang L, Wan G, Zhang X, Wang Y and Zhao G (2023). Depleted miR-125a-5p causes vascular endothelial cell dysfunction in deep vein thrombosis by targeting angiopoietin 2. *Indian J. Hematol. Blood Transfus*., **39**(1): 116–122.

Klontz E, Obi JO, Wang Y, Glendening G, Carr J, Tsibouris C, Buddula S, Nallar S, Soares AS, Beckett D, Redzic JS, Eisenmesser E, Palm C, Schmidt K, Scudder AH, Obiorah T, Essuman K, Milbrandt J, Diantonio A, Ray K and Snyder GA (2023). The structure of NAD+ consuming protein *Acinetobacter baumannii* TIR domain shows unique kinetics and conformations. *J. Biol. Chem*., **299**(11): 105290.

Leibler C, Thomas KB, Josensi C, Levack RC, Smita S, John S, Wikenheiser DJ, Bastacky S, Gingras S, Nickerson KM and Shlomchik MJ (2025). Divergent TIR signaling domains in TLR7 and TLR9 control opposing effects on systemic autoimmunity. *J. Clin. Invest*., **135**(21): e189566.

Lin YC, Huang YL, Wang MH, Chen CY, Chen WM, Weng YC and Wu PY (2022). Calreticulin regulates β1-integrin mRNA stability in PC-3 prostate cancer cells. *Biomedicines*., **10**(3): 646.

Li F, Cao K, Wang M, Liu Y and Zhang Y (2022). Astragaloside IV exhibits anti-tumor function in gastric cancer via targeting circRNA dihydrolipoamide S-succinyltransferase (circDLST)/miR-489-3p/eukaryotic translation initiation factor 4A1(EIF4A1) pathway. *Bioengineered*., **13**(4): 10111–10122.

Ma Q, Lu X, Tian W, Chen Y and He X (2024). Astragaloside IV mediates the effect and mechanism of KPNB1 on biological behavior and tumor growth in prostate cancer. *Heliyon*., **10**(13): e33904.

Sheng W, Ding J, Liu L, Wang N, Lu B, You X, He Q and Zhou Q (2022). Curcumol inhibits the development of prostate cancer by miR-125a/STAT3 axis. *Evid. Based Complement. Alternat. Med*., **2022**: 9317402.

Tian H, Zhang T, Qin S, Huang Z, Zhou L, Shi J, Nice EC, Xie N, Huang C and Shen Z (2022). Enhancing the therapeutic efficacy of nanoparticles for cancer treatment using versatile targeted strategies. *J. Hematol. Oncol*., **15**(1): 132.

Tavakoli Z, Khajeh K and Ranjbar B (2026). A hybrid nanosystem for prostate cancer therapy: Codelivery of enzalutamide and curcumin via selenium-embedded mesoporous silica and chitosan nanoparticles. *Chemistry Open*., **15**(3): e202500589.

Van Blarigan EL, McKinley MA, Washington SL, 3rd Cooperberg MR, Kenfield SA, Cheng I and Gomez SL (2025). Trends in prostate cancer incidence and mortality rates. *JAMA Netw. Open*, **8**(1): e2456825.

Vallejo-Schmidt T, Palm C, Obiorah T, Koudjra AR, Schmidt K, Scudder AH, Guzman-Cruz E, Ingram LP, Erickson BC, Akingbehin V, Riddick T, Hamilton S, Riaz T, Alexander Z, Anderson JT, Bader C, Calkins PH, Chaudhry SS, Collins H, Conteh M and Snyder MLD (2024). Characterization of the structural requirements for the NADase activity of bacterial Toll/IL-1R domains in a course-based undergraduate research experience. *Immunohorizons*., **8**(8): 563–576.

Wu B and Liao SG (2025). The histone deacetylase inhibitor CG-745 enhances the radiosensitivity of prostate cancer cells. *J. Int. Med. Res*., **53**(9): 3000605251371562.

Wu T, Wu S, Gao H, Liu H, Feng J and Yin G (2024). Astragaloside IV augments anti-PD-1 therapy to suppress tumor growth in lung cancer by remodeling the tumor microenvironment. *Eur. J. Histochem*., **68**(4):

Article in Press

4098.

Xiao Y, Zhong L, Liu J, Chen L, Wu Y and Li G (2024). Progress and application of intelligent nanomedicine in urinary system tumors. *J. Pharm. Anal*., **14**(12): 100964.

You X, Wu Y, Li Q, Sheng W, Zhou Q and Fu W (2022). Astragalus-scorpion drug pair inhibits the development of prostate cancer by regulating GDPD4-2/PI3K/AKT/mTOR pathway and autophagy. *Front. Pharmacol*., **13**: 895696.

You X, Qiu J, Li Q, Zhang Q, Sheng W, Cao Y and Fu W (2024). Astragaloside IV-PESV inhibits prostate cancer tumor growth by restoring gut microbiota and microbial metabolic homeostasis via the AGE-RAGE pathway. *BMC Cancer*., **24**(1): 472.

Yang H, Qu Y, Tian Y, Wang C, Sun Y, Dai Z, Yue X and Cheng W (2024). Ultrasound-targeted microbubble destruction enhances the inhibitory effect of sonodynamic therapy against hepatocellular carcinoma. *ACS Omega*., **9**(52): 51253–51263.

Zhu H, Zheng L, Zhao K, Wang X, Ma Z, Zeng A, Zhao W, Zhang W, Han L and Huang Y (2025). Astragaloside IV improves diabetic kidney disease by regulating NLRP3 inflammasome. *J. Diabetes Res*., **2025**: 3340719.

Zhu Z, Cao Y, Liu L, Zhao Z, Yin H and Wang H (2022). Atorvastatin regulates the migration and invasion of prostate cancer through the epithelial-mesenchymal transformation and matrix metalloproteinase pathways. *Investig. Clin. Urol*., **63**(3): 350–358.

Zhu X, Yin X, Niu L, Yang G, Xu Y, Yu Y, Cheng Y, Ma X, Huang T, Wei W and Tao F (2025). Cerium oxide-embedded gold nanoparticles loaded with astragaloside IV for bladder cancer therapy. *Sci. Rep*., **15**(1): 36067.

Zhu Y and Lu F (2024). Astragaloside IV inhibits cell viability and glycolysis of hepatocellular carcinoma by regulating KAT2A-mediated succinylation of PGAM1. *BMC Cancer*., **24**(1): 682.

Article in Press